

UC Berkeley

UC Berkeley Previously Published Works

Title

Impact of Platinum Primary Particle Loading on Fuel Cell Performance: Insights from Catalyst/Ionomer Ink Interactions

Permalink

<https://escholarship.org/uc/item/3vn5z58j>

Journal

ACS Applied Materials & Interfaces, 14(32)

ISSN

1944-8244

Authors

Berlinger, Sarah A
Chowdhury, Anamika
Van Cleve, Tim
[et al.](#)

Publication Date

2022-08-17

DOI

10.1021/acsami.2c10499

Peer reviewed

Impact of platinum primary-particle loading on fuel-cell performance: Insights from catalyst/ionomer ink interactions

Sarah A. Berlinger^{‡ 1,2}, Anamika Chowdhury^{‡ 1,2}, Tim Van Cleve³, Aaron He^{1,2}, Nicholas Dagan^{1,2}, Kenneth C. Neyerlin³, Bryan D. McCloskey^{1,2}, Clayton J. Radke¹, and Adam Z. Weber²

¹Department of Chemical and Biomolecular Engineering, University of California, Berkeley, Berkeley, CA 94720 USA

²Energy Technologies Area, Lawrence Berkeley National Laboratory, Berkeley, CA 94720 USA

³Chemistry and Nanoscience Center, National Renewable Energy Laboratory, Golden, CO 80401 USA

Corresponding Author

*Adam Z. Weber: azweber@lbl.gov

Author Contributions

[‡]These authors contributed equally

KEYWORDS: Polymer Electrolyte Fuel Cell, Inks, Colloidal Interactions, Electrode Fabrication, platinum, Nafion

ABSTRACT

A variety of electrochemical energy-conversion technologies, including fuel cells, rely on solution-processing techniques (via inks) to form their catalyst layers (CLs). The CLs are heterogeneous structures, often with uneven ion-conducting polymer (ionomer) coverage and underutilized catalyst. Various platinum-supported-on-carbon colloidal catalyst particles are used, but little is known about how or why changing the primary particle loading (PPL, or weight fraction of platinum of the carbon-platinum catalyst particles) impacts performance. By investigating CL gas-transport resistance and zeta (ζ) potentials of corresponding inks as a function of PPL, a direct correlation between CL high-current-density performance and ink ζ -potential is observed. This correlation stems from changes in ionomer distributions and catalyst-particle agglomeration as a function of PPL as revealed by pH, ζ -potential, and impedance measurements. These findings are critical to unraveling ionomer distribution heterogeneity in ink-based CLs and enabling enhanced Pt utilization and improved device performance for fuel cells and related electrochemical devices.

INTRODUCTION

Polymer-electrolyte fuel cells (PEFCs) present an attractive clean-energy alternative to conventional energy sources in several energy sectors, especially heavy-duty transportation. However, widespread commercialization is limited due to the high costs associated with the use of platinum (Pt) in the catalyst layers (CLs). Unfortunately, reducing overall Pt loading induces significant transport losses and poor performance, particularly gas-transport losses in the cathode CL.¹⁻² Mitigating these losses, while maintaining low Pt loadings, is paramount to the widespread deployment of PEFC technology.

CLs in PEFCs are complex porous-electrode structures consisting of agglomerates of Pt-supported-carbon catalyst particles (collectively referred to here as catalyst particles) and ion-conducting polymer (ionomer) binder.³⁻⁴ The catalyst particles are roughly 30-50 nm in diameter (determined primarily by the size of the carbon support) and are decorated with 2-4 nm platinum nanoparticles. The carbon, platinum, ionomer, and void-space pathways create a triple-percolated network for the transport of various species to and from the reaction sites: reactant gas (H_2 , O_2), product water, protons (H^{+}), and electrons (e^{-}). Using microscopy,⁵⁻¹⁰ ptychography,¹¹ and tomography,¹²⁻¹⁴ studies have revealed the heterogeneous nature of CL structures: there are non-uniform ionomer distributions (with a significant fraction of Pt not in direct contact with ionomer), isolated ionomer domains, and wide variety of agglomerate (defined here as aggregates of catalyst particles plus ionomer) sizes and ionomer film thicknesses. The total platinum loading in a CL reported in mg_Pt/cm^2 , and the ionomer-to-particle weight ratio (typically expressed as ionomer-to-carbon ratio, I:C) are two commonly studied CL fabrication parameters.^{1, 12, 15-18} Of note, in addition to varying total platinum loading, platinum loading on the carbon-support particles (termed primary particle loading, PPL) can also change. Notably, higher PPL results in larger Pt nanoparticle sizes.¹⁹⁻²⁰ When platinum nanoparticles are not near or in contact with the ionomer, they do not contribute to the electrochemical surface area (ECSA). Optimization of CL structure with well-distributed phases is essential to allow for efficient species transport and high Pt utilization (and therefore high current densities and reduced capital costs).

CLs are fabricated from inks containing catalyst particles and ionomer dispersed in solvent (typically water:alcohol mixtures). The interactions between the components in solution govern how these agglomerates (aggregates of catalyst particles and ionomer) self-assemble, including how the ionomer adsorbs to the catalyst particles.²¹⁻²³ Upon drying, ink-level interactions manifest and control the eventual CL microstructure, the nature of the ionomer/catalyst-particle interface, and the properties of the ionomer.^{3, 21, 24-29} Ink properties (*e.g.*, ink zeta potential, ζ , and agglomerate size distribution) correlate well with CL performance (*e.g.* mass activity and gas-transport resistance) as a function of ink water:alcohol ratio²⁴ and I:C ratio.³⁰ Importantly, the surface chemistry of the catalyst particles (*i.e.*, platinum-nanoparticle loading and distribution and carbon type) alters how the ionomer interacts with them, as evidenced by rheological measurements.³¹ Furthermore, calorimetry and ionomer-adsorption measurements reveal that, when subject to no applied potentials, binding strengths of ionomer are higher on hydrophobic (carbon) surfaces than on platinum surfaces when using Nafion (a prototypical ionomer, although depending on ionomer charge density the magnitude of this relationship may change).³² One therefore expects that as the PPL varies (*i.e.*, the surface area of platinum nanoparticles relative to carbon particles), ionomer/catalyst-particle interaction strengths differ (decreasing interaction with increasing platinum surface area), which could impact device power output. While changing total Pt loading is well studied^{1, 15, 33}, varying Pt distributions within the CL caused by differing PPL is poorly understood.

In this study, we probe the influence of PPL on both ink and CL properties, using Vulcan carbon-supported particles and Nafion as a model support and ionomer, respectively. Vulcan is chosen as a model support due to its very low internal porosity; changes in PPL, therefore, can be directly correlated with differences in the platinum versus carbon surface area on the exterior of the catalyst particle. Ink ionomer/catalyst-particle interactions are explained with ζ -potential and pH measurements as a function of I:C. We link ink interactions to CL properties by investigating both gas-transport resistance and ζ -potential of corresponding inks as a function of PPL. Additionally, CL findings are validated by double-layer capacitance and H^{+} transport-resistance measurements. In this way, we probe the influence of carbon and platinum surface area on ink properties to understand how they determine CL transport, revealing important

implications for controlling ionomer and catalyst-particle distribution heterogeneity and consequently improving Pt utilization.

EXPERIMENTAL

Ink preparation and measurements: Inks for electrode fabrication were prepared by dispersing ionomer dispersions[‡] (Nafion®, D521, Ion Power, Delaware, USA) and Pt-nanoparticle catalyst supported on Vulcan carbon (TEC10V10E, TEC10V30E and TEC10V50E from TKK, Tokyo, Japan) in a solvent mixture of 18 M Ω deionized water (Millipore Milli-Q® IQ 7000 Water Purification System, Millipore Sigma, Massachusetts, USA) and *n*-propyl alcohol (>99.9 % purity, Sigma Aldrich, Missouri, USA) in a 1:1 weight ratio. For the bare carbon samples, Vulcan XC72 was used (Fuel Cell Store, Texas, USA). The carbon-to-solvent weight ratio was kept constant at 0.03 wt. % for low Pt-loading electrode samples (0.05 mg/cm² electrode geometric surface area) and zeta-potential measurements. For higher Pt-loading samples (0.1 mg/cm² electrode area), the carbon-to-solvent weight ratio was increased to 0.1 wt.%. All inks were manually agitated followed by sonication for 30 minutes in a bath sonicator (Branson, Connecticut, USA) maintained at 10°C using a water recirculatory/chiller (F25-HL Refrigerated - Heating Circulator, Julabo Inc, Pennsylvania, USA). Zeta potentials of the inks were measured immediately after sonication via electrophoretic light scattering (NanoPlus3, Micromeritics, Georgia, USA), modeled using the Smoluchowski equation.³⁴ To elucidate ionomer/catalyst-particle interactions in inks, pH measurements were conducted over a wide range of I:C ratios. Inks were prepared in a similar manner as above, with a fixed carbon-to-solvent ratio of 0.1 wt. %, dispersed in varying ionomer concentrations using solvent-diluted ionomer (Nafion®, D2021, Ion Power, Delaware, USA). pH measurements were taken with an Orion Star A211 pH meter and a ROSS Ultra Triode pH probe with automatic temperature compensation (Thermo Fisher

^{‡‡} Consistent with the terminology in the field, we use the term ionomer “dispersion” to mean an ionomer and solvent system. Importantly however, given the ζ trends presented herein, “solution” may be a more appropriate term based on observed tendency of the ionomer to uniformly distribute in the ink at high I:C and control “bulk” behavior.

Scientific, Massachusetts, USA). The probe was calibrated before each use with appropriate known standards. Samples were stirred at 400 RPM for the course of the pH measurement. Most samples equilibrated in less than 30 s.

Electrode fabrication: Electrodes were prepared by spray coating inks using a Sono-Tek ultrasonic spray coater and a 25 kHz AccuMist nozzle (Sono-Tek Exacta Coat, New York, USA). The working electrode (WE) was spray-coated onto a NR212 Nafion membrane (Ion Power, Delaware, USA) while the counter electrode (CE) was spray-coated onto a gas-diffusion layer (GDL) (Sigracet 25BC, SGL Wiesbaden, Germany). In the WE, the total Pt mass loading was maintained at 0.05 mg/cm² and 0.1 mg/cm² for CL gas-transport resistance and electrochemical impedance spectroscopy (EIS) measurements, respectively. CE utilized a total Pt loading of 0.3 mg/cm². Nafion ionomer binder at an I:C ratio of 0.7 and 0.9 was utilized for all WEs and CEs, respectively.

Cell assembly for CL gas-transport resistance measurements: Membrane-electrode assemblies (MEAs) were prepared by stacking the CE sprayed onto the GDL against a Nafion membrane (NR-212, ~50 μm thickness) with the WE sprayed on the other side. Additional GDL sheets were added on the WE-side during measurements. The active cross-sectional area, determined by the WE electrode cross-sectional area directly in contact with the GDL, was limited to 2 cm². The remaining area was covered by impermeable Teflon gaskets (PTFE, McMaster Carr, Illinois, USA) to prevent gas exposure, seal the cell, and achieve the desired GDL compression. The entire assembly was mounted in a single cell with graphite flow-fields (total area 5 cm²) and single serpentine flow channels (Fuel Cell Technologies Inc, New Mexico, USA). The cell was operated using a commercial test stand (850e Multi-Range Fuel Cell Test System, Scribner Associates, North Carolina, USA) that allowed control of gas flowrates, humidity, cell temperature, and cell backpressure. Cyclic voltammograms (CVs) and limiting-current measurements were recorded via a Biologic VSP potentiostat (Biologic, Seyssinet-Pariset, France).

Cell assembly for electrochemical impedance spectroscopy (EIS) and polarization-curve measurements: MEAs described above were sandwiched between two 25-cm² SGL29 BC GDLs,

at 25% compression and placed between the flow fields with the cell bolts tightened to 40 in-pounds. 25-cm² double/triple (CE/WE) serpentine flow fields were used.

Break-in protocol: A modified version of the break-in protocol described by Ono *et al.*³⁵ was adopted for this study. The samples were maintained at a constant potential (0.2 V referenced to the CE) for 12 h at 80°C, 100% relative humidity (RH), and 50 kPa gauge pressure while flowing pure H₂ (flowrate of 400 standard cubic centimeters per minute, SCCM) on the CE side and air (flowrate of 800 SCCM) on the WE side.

Electrochemical surface area (ECSA) measurement: ECSA was estimated by CO-stripping voltammetry as described by Schuler *et al.*³⁶ at 40°C, 80% RH, and ambient pressure (same operating conditions for the limiting-current measurements). Briefly, both electrodes were flushed using humidified Ar for 1 h to hydrate the sample at the desired RH. The CE feed was then switched to 2% H₂ in Ar, and 20 cleaning cycles were performed between 0.08 to 0.95 V (referenced to the CE) at a scan rate of 50 mV/s, followed by additional 20 cleaning cycles over the same potential range at a scan rate of 100 mV/s. The WE was thereafter fed with 1% CO diluted in Ar at 500 SCCM for CO adsorption for 5 min to allow CO adsorption. Next, Ar purged the WE at 500 SCCM for 15 min to remove excess CO and obtain an irreversibly adsorbed monolayer. Finally, three CVs were recorded by sweeping the WE potential between 0.08 to 0.95 V (referenced to CE) at a scan rate of 100 mV/s. ECSA was calculated from the charge integration of the CO peak. The second and third CVs served as a baseline for charge integration of the CO peak. A CO-monolayer oxidation charge of 420 mC/cm² was assumed in all calculations.³⁷ The surface-area roughness factor r_f , commonly used to characterize electrodes and defined as the ECSA normalized to electrode geometric area,² was estimated from the ratio of ECSA to WE active area (2 cm²). r_f values are reported in the Supporting Information (SI).

Transport-resistance measurement: Electrode transport resistances were ascertained from limiting-current measurements using the H₂-pump configuration and test protocol as described by Spingler *et al.*³⁸ and Schuler *et al.*³⁶ A 2 vol.% H₂ in Ar mixture was fed to the CE to minimize crossover current while maintaining a stable potential. To achieve the mass-transport limit of the WE, low-concentration gas mixtures of 1000 ppm H₂ in Ar were utilized. The flowrates

maintained were 1000 standard cm³/min on the WE and 500 standard cm³/min on the CE. The setup was maintained at 40°C, 80 % RH, and ambient pressure during the measurements.

To record the limiting current, the cell was flushed using humidified Ar for 45 min. The CE feed was then switched to 2 vol.% H₂ in Ar, and 20 cleaning cycles were performed between 0.08 to 0.95 V (referenced to CE) at a scan rate of 50 mV/s, followed by an additional 20 cleaning cycles over the same potential range at scan rate of 100 mV/s. Thereafter, the potential on the WE was maintained constant at 0.3 V (referenced to the CE) to record the crossover current. The WE gas was then switched to 1000 ppm H₂ to record the total steady-state current density. To reach limiting current, voltage was increased until the current remained constant. Limiting current density at this point was then obtained by subtracting the crossover current density from the total current density.²

The total cell resistance R_{Total} is given by the ratio of average feed reactant concentration (on the WE) to the measured limiting current i_{lim} as

$$R_{Total} = \frac{nF C_{Feed}^{Avg}}{i_{lim}} \quad (1)$$

where n is the number of electrons in the overall reaction. R_{Total} for the H₂-pump configuration is composed of transport resistances from the GDL and the WE,

$$R_{Total} = N R_{GDL} + R_{CL} \quad (2)$$

where N is the number of GDLs stacked on the WE, R_{GDL} is the transport resistance of a single GDL, and R_{CL} is the WE transport resistance. R_{GDL} is determined from GDL stacking experiments where R_{Total} is measured as a function of N keeping other system parameters constant.³⁸ The slope of R_{Total} versus N represents R_{GDL} . R_{CL} is determined by subtracting the total GDL resistance $N R_{GDL}$ from R_{Total} . Measurement precision is maintained since the magnitudes of R_{CL} , $N R_{GDL}$, and the difference between the two are much higher than experimental error.

Impedance measurements: EIS experiments were prepared on fully conditioned 25 cm² MEAs with WE-Pt loading of 0.1 mg Pt/cm² using a Gamry Reference 3000 Potentiostat connected to a

Gamry 30k Booster. EIS experiments were conducted at 80°C with 1 atm pure H_2 and N_2 flowing at 100 SCCM at CE and WE gas lines, respectively. Experiments were run at 10, 25, 50, 75, and 100 % RH with 30 to 60 min equilibration before each measurement. EIS was measured over 50 kHz to 100 mHz at 0.45 and 0.2 V versus RHE with ± 10 mV oscillations for CO-free and CO-doped experiments, respectively. The WE was exposed to 1 vol.% CO/ N_2 feed for 15 min to allow for CO adsorption, then purged with pure N_2 prior to CO-doped experiments. Residual CO was oxidized after CO-doped EIS experiments and before CO-free EIS measurements via CO stripping voltammetry.

The CL ionic sheet resistance (R_{sheet}) was determined by fitting EIS data (between 50 kHz and 0.1 Hz) from 100% RH- H_2/N_2 EIS spectra to a spherical diffusion model³⁹ (Equation (3)) with an Open Source Impedance Fitter (OSIF)⁴⁰ tool,

$$Z = (i\omega)^\theta l + R_{hfr} + \frac{R_{sheet}}{\sqrt{R_{sheet} C_{dl}} (i\omega)^\phi \coth \sqrt{R_{sheet} C_{dl}} (i\omega)^\phi - 1} \quad (3)$$

where Z is complex impedance, l is inductance of nonideal inductor, ω is frequency (rad/s), R_{hfr} is a high frequency resistance element, R_{sheet} is CL sheet resistance, C_{dl} is the double-layer capacitance of a nonideal capacitor, and θ, ϕ are power index phase elements between 0 and 1 representing nonideal inductor and capacitor behavior, respectively. A value of 1 corresponds to an ideal constant-phase element. Due to the relative thinness of the CLs, the spherical diffusion model (Equation (3)) gave better fits compared to an analogous transmission-line model with capacitive and inductive elements modeled as constant-phase elements. Table S4 presents the values of each variable fit in Equation 3.

Ionomer fractional capacitance (or the dry divided by the wet capacitance of the CL) is attributed to changes in ionomer coverage and was determined on both Pt and C surfaces by comparing the changes in C_{dl} taken under wet (80-100% RH) and dry (10% RH) conditions with and without CO exposure, as previously described.^{24, 37} The presence of CO helps isolate the platinum from the carbon capacitance contribution. C_{dl} for an individual EIS spectrum was determined by finding the y-intercept of ω^{-2} vs $-1/\omega Z_{img}$ plot using the linear region present at low frequency (typically 0.1 to $0.5 < \omega^{-2} < 2.5$ rad²/s²). This method was used for all conditions (wet, dry, with

and without CO) rather than using the results of Equation 3 because the spherical-diffusion model gave poor fits under dry conditions. However, the wet-condition values for C_{dl} were very similar when comparing the two methods. Uncertainty of the y -intercept associated with the least-square linear-regression fit were propagated through all calculations.

H₂/air polarization curves: The cell was maintained at 80°C, 150 kPa total pressure and varying RH. H₂ and air were fed to the CE and WE, respectively. The test protocol involved measuring the current-versus-voltage curves from 0.3 V to open-circuit voltage (OCV) for 4 min per point (average of last 1 min used). Currents were normalized by ECSA to account for differences in Pt surface area with varying PPL loading.

SEM imaging (electrode and electrode thickness): SEM images of the CLs were obtained using a SEM FEI Quanta 250 FEG equipped with a Bruker Quantax 200 EDX detector. For CL-thickness measurements, the samples were freeze-fractured under liquid nitrogen. Average thickness (and associated images) from three different CL locations is reported in the SI in Table S5.

RESULTS & DISCUSSION

Ink Characterization. Varying the PPL changes the relative amounts of carbon and Pt surface area of catalyst particles: estimates indicate that the carbon surface area decreases from 100 to 70-80% when the Pt surface area increases from 0% to 20-30% as Pt PPL increases from 0 to 46 wt.% (see SI). It is worth noting that the surface area does not vary linearly with Pt-nanoparticle loading because carbon and Pt have drastically different specific (mass-normalized) surface areas (see Table S1-2). Additionally, because Pt is slightly hydrophilic and Vulcan carbon (C) is slightly hydrophobic, varying PPL alters the hydrophobic/hydrophilic nature of catalyst particle surfaces, thereby influencing ionomer adsorption onto the catalyst particles.³²

ζ -potential can be thought of as an effective surface potential of the agglomerates in the ink and therefore is an indicator of colloidal stability: keeping all other variables constant, high magnitude ζ -potential particles experience more electrostatic repulsion and therefore tend to

aggregate less than low ζ -potential particles. It has previously been established that ζ -potential is closely coupled with I:C ratio,³⁴ indicating the ζ -potential strongly depends on ionomer/catalyst-particle interactions. Therefore, it is expected that the dependence of ζ -potential on I:C ratio changes as a function of PPL. To probe this assertion, Figure 1 shows the ink ζ -potential as a function of I:C ratio (Nafion is used as the ionomer) for 0 (bare C), 10, and 30 wt.% Pt on C. A 1:1 water:*n*-propanol solvent composition is used for all inks in this study. In Figure 1, ζ -potential exhibits a U-shaped dependence on the I:C ratio for the three PPLs; Figure S1 also plots ζ -potential for a much wider range of I:C using bare carbon support particles (0 wt.% Pt). Generally, ζ -potential is proportional to the surface charge density on a particle and inversely proportional to the square root of the ionic strength of the surrounding medium.⁴¹ Although this is a non-classical system (no added electrolyte), the general trends with surface charge and ionic strength still hold (discussed more in the SI).

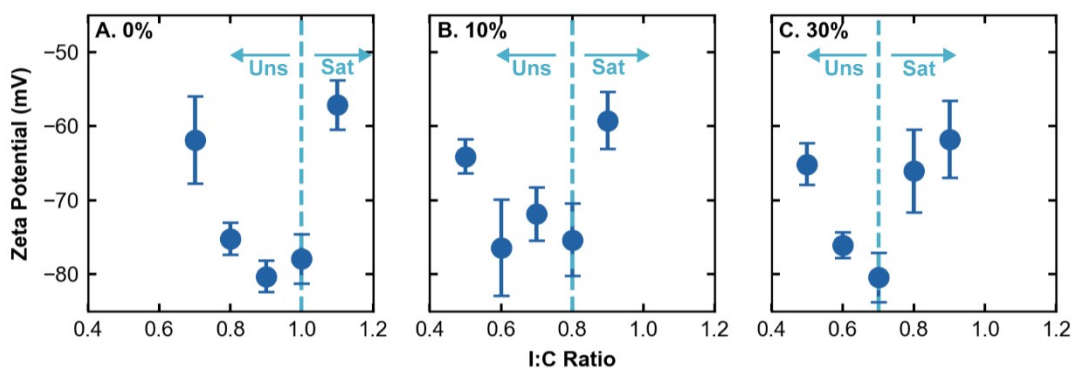


Figure 1. Zeta potential of inks of varying ionomer-to-carbon (I:C) ratios, containing (A.) 0 wt.% Pt bare-carbon-support particles, and (B.) 10 wt.% Pt, or (C.) 30 wt.% Pt-on-carbon catalyst particles. The dashed light blue vertical lines indicates where the marginal ionomer added switches from adsorbing to the particle surface (because the surface is unsaturated, Uns) to no longer adsorbing (because the surface is saturated, Sat). (B.) and (C.) are reproduced with permission from reference³⁰ Copyright 2021 American Chemical Society. Error bars display the standard deviation of multiple replicate samples.

We first examine the initial part of the U-shaped curve at low I:C ratios in Figure 1A. In a dispersion, the acid group in the sulfonate sidechain dissociates to solubilize H^{+} ions and

negatively charged SO_3^- groups (the sulfonate groups should be almost fully dissociated in this environment).^{34, 42} The increase in ζ -potential magnitude (more negative) indicates that the catalyst/carbon-particle agglomerates are becoming more negatively charged. In other words, ionomer adsorption onto the catalyst/carbon-particle agglomerate surface likely initially causes a more negative ζ as I:C increases due to negatively charged SO_3^- groups associated with the adsorbed ionomer. This initial increase in ζ -potential magnitude cannot be due to addition of non-adsorbing ionomer; if the ionomer did not adsorb, it would increase the surrounding ionic strength and cause the opposite trend. Similarly, the increase cannot be due to the ionomer itself, because the ζ -potential of pure Nafion in this solvent is difficult to interpret (indeterminate via electrophoretic light scattering).

At a certain I:C ratio however, the ζ -potential value stops becoming more negative, and instead decreases in magnitude with additional ionomer. We here define the transition ratio based on the data of Figure 1 corresponding to the last data point following the first half of the U-shaped curve (*i.e.* the inflection point). This I:C transition ratio occurs at ionomer adsorption saturation as confirmed by independent adsorption studies.^{32, 43} After the I:C transition, additional ionomer in solution behaves like small-molecule salts and acids (Figure S1B): the catalyst/carbon-particle agglomerate surfaces are adsorption saturated with ionomer, and dissociated H^+ ions from the additional ionomer increase the ionic strength of the surrounding solvent medium. The increase in ionic strength causes ζ -potential to trend toward zero.

Interestingly, the I:C transition ratio is a function of PPL. For bare carbon (0% Pt, Figure 1A), the transition occurs at an I:C of 1. As PPL increases, the transition point progressively shifts to lower I:C ratios: 0.8 for 10 wt.% Pt and 0.7 for 30 wt.% Pt, as indicated by the light-blue dashed vertical lines in Figure 1. Nafion adsorbs more strongly onto Vulcan carbon than onto Pt nanoparticles under similar conditions in the ink.³² As the carbon SA available for the ionomer to interact with decreases (Table S1-2), the amount of ionomer the catalyst-particle surface can accommodate also decreases, in agreement with the decreasing threshold I:C with increasing PPL.

To explore the relationship between PPL and ionomer/particle ink interactions further, pH is measured during ink titration with ionomer,³⁴ and compared with the pH of ionomer-only

dispersions at the same ionomer concentrations. The pH of both the ink (with 0, 30, and 46 wt.% Pt/C catalyst particles) and the Nafion dispersion (no catalyst particles) are plotted on the y - and x -axes, respectively in Figure 2; the raw data of ink pH versus I:C is given in Figure S3.

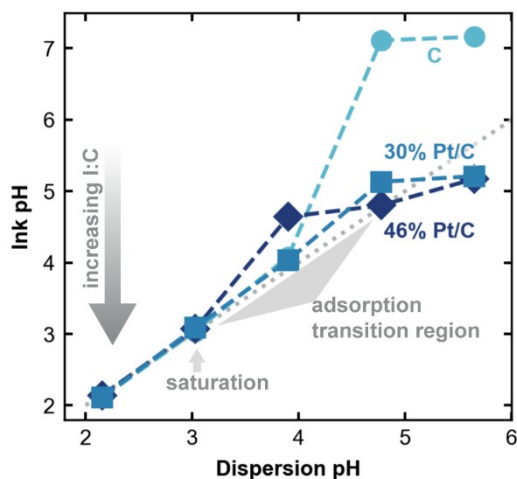


Figure 2. Measured pH titrating of an ink containing either bare carbon (C), 30, or 46 wt.% platinum on carbon (Pt/C) as a function of the measured pH of ionomer-solvent dispersions of the same composition containing no particles. Dashed lines are guides for the eye. The dotted gray line indicates a one-to-one correlation.

We first examine the bare-carbon data (light blue circles in Figure 2). Because the ionomer is acidic, low pH values (bottom left of Figure 2) represent the highest ionomer concentrations (highest I:C). In this regime, the pH of the ink and the ionomer dispersions agree directly, thus indicating that the ionomer contributes to the bulk pH in a similar manner with and without catalyst particles. However, at low ionomer concentrations (top right of the figure), a clear deviation from this linear behavior (evidenced by a slope change) between the ink and dispersion pH is observed. This difference could be due to the carbon-support particles or to ionomer/carbon-particle interactions. Initial ink pH values (top right of the graph) are set by the solvent/carbon-particle environment. Notably, the ink pH in this region is relatively insensitive to ionomer concentration when ionomer is first increased. Figure S3 replots the ink pH data as a function of I:C. This insensitivity is because the ionomer does not contribute to the bulk pH in

this region, suggesting that it is bound/adsorbed to the carbon particle. This indicates that the H^+ counterions located in the adsorbed layer do not distribute freely into the bulk solution, and accordingly, do not significantly impact bulk solution pH. However, as more ionomer adsorbs to the agglomerates as indicated by the changing slope region from pH ~3-6, the ink and dispersion pH values eventually converge. When they do converge (around pH ~3, corresponding to similar I:C values as in Figure 1 as shown in Figure S3) the carbon particles are adsorption saturated. Here, additional ionomer in the solution contributes to the bulk pH as it would in an ionomer-only dispersion. Therefore, deviation between ink and dispersion pH is due to adsorption of the ionomer to the carbon-particle surface; pH may be thought of as a measure of bulk (free) ionomer.

This same trend is seen for the Pt/C data: all inks display relatively insensitive pH responses with increasing ionomer concentration at low I:C ratios. The Pt/C values are also initially more acidic than bare carbon support due to differences in surface chemistry induced by the acidic platinum deposition process.[‡] For the Pt/C ink pH data, adsorption of ionomer onto the catalyst particles scavenges ionomer from solution. Below pH ~3, enough ionomer is present to overcome adsorption loss of solution ionomer onto the catalyst particles.

In our inks, the fact that ionomer does not contribute to bulk pH at low ionomer concentrations (likely due to interactions with the catalyst/carbon-particle surface) and does so at high concentrations corroborates the U-shaped ζ -potential behavior, in which at low concentrations the ionomer does not add to ionic strength but rather lowers ζ -potential due to adsorption. At high ionomer concentrations, the additional ionomer (beyond the adsorption saturation point) remains dispersed in the solvent, thereby increasing the bulk ionic strength. Furthermore, the pH transition region occurs at similar I:C ratios (Figure S3) as the ζ -potential-transition values. It is important to note that the observed ζ -potential trend may not hold for inks with very low carbon concentrations (*i.e.*, where the amount of ionomer adsorbed to the carbon surface area negligibly affects bulk ionomer concentration).

[‡] It should be noted therefore that the bare carbon did not undergo a similar treatment process, and the ionomer/carbon interactions are likely inherently slightly different between untreated bare carbon and the carbon. The data are presented here, however, to understand the intrinsic ionomer/Vulcan interaction.

CL Characterization. To understand how PPL-influenced ink interactions affect CL performance, CLs made from inks comprised of catalyst particles of varying PPL (bare C (0% Pt), 10, 30, and 46 wt% Pt/C catalysts) but identical I:C ratios were fabricated and tested, where the total platinum loading and solvent composition (1:1 water:*n*-propanol) and other fabrication procedures remaining identical. A fixed I:C of 0.7 was chosen to capture behavior on either side of the ζ -transition value for the varying PPLs (*i.e.*, 10% should be to the left of, 30% should be on, and 46% should be to the right of the transition values as seen in Figure 1). Because ionomer interacts more strongly with carbon rather than with platinum,³² the available SA of the Pt/C catalyst particle for ionomer to adsorb decreases as the platinum weight fraction on the particle increases. Consequently, we expect the ionomer distribution on the catalyst-particle surface to be more heterogeneous and spatially separated by platinum nanoparticles as PPL increases. Importantly, in the following data, the total platinum loading is maintained constant (0.05 mg/cm²) across all samples; only the PPL changed, and thus performance differences are due to differences in PPL. PPL differences yield differences in Pt (and ionomer) distributions in the CL and CL thickness/porosity. In the subsequent analysis we attempt to isolate the first effect by normalizing for the latter one, as described below. Note that these PPL data are fundamentally different from those of previous studies investigating the effect of total platinum loading¹ and the two situations should not be confused.

Figure 3A shows the effect of PPL on CL gas-transport resistance and corresponding ink ζ -potential. Gas transport was not measured for bare carbon because it is a poor H₂ catalyst. CL gas-transport resistance is composed of the total transport resistance for the gas to diffuse through the CL thickness to the Pt reaction sites. At low Pt CL loadings (as is the case here), the overall CL gas-transport resistance is dominated by local gas-transport resistance which is composed of ionomer thin-film transport resistance and an interfacial resistance at the Pt/ionomer interface.² Because total platinum loading was the same for all CLs, each CL had a different nominal thickness due to the varying PPL used: CLs fabricated from high PPL have less total carbon, and are, therefore, thinner. Additionally, ECSA varied widely across the CLs with different PPL (Table S3). This probably results from changes in Pt nanoparticle size as a function

of PPL.¹⁹⁻²⁰ The CL gas-transport-resistance data presented in Figure 3A are, therefore, normalized to the average ECSA (see SI).

As mentioned above, ζ -potential correlates well with CL high current-density performance.^{24, 30} Changes in CL structure are triggered by differences in ionomer/catalyst-particle interactions. In Figure 3, we also see a strong relationship between transport resistance and ζ -potential as a function of PPL. CLs with low PPL exhibit low CL gas-transport resistance and high ζ -potential magnitudes. At 46 Pt wt.% PPL, a sharp increase in CL gas-transport resistance occurs concurrently with a sharp decrease in ζ magnitude. The gas-transport-resistance data agree with previous studies that report decreases in CL high-current-density performance with increased PPL.⁴⁴ The previous literature attribute these trends to crowding of the carbon surface by Pt nanoparticles, resulting in a low flux per Pt nanoparticle.⁴⁴ However, the coinciding ζ -potential trends here with high gas-transport resistances suggest microstructural changes of the CL toward apparently larger catalyst-particle agglomerates.

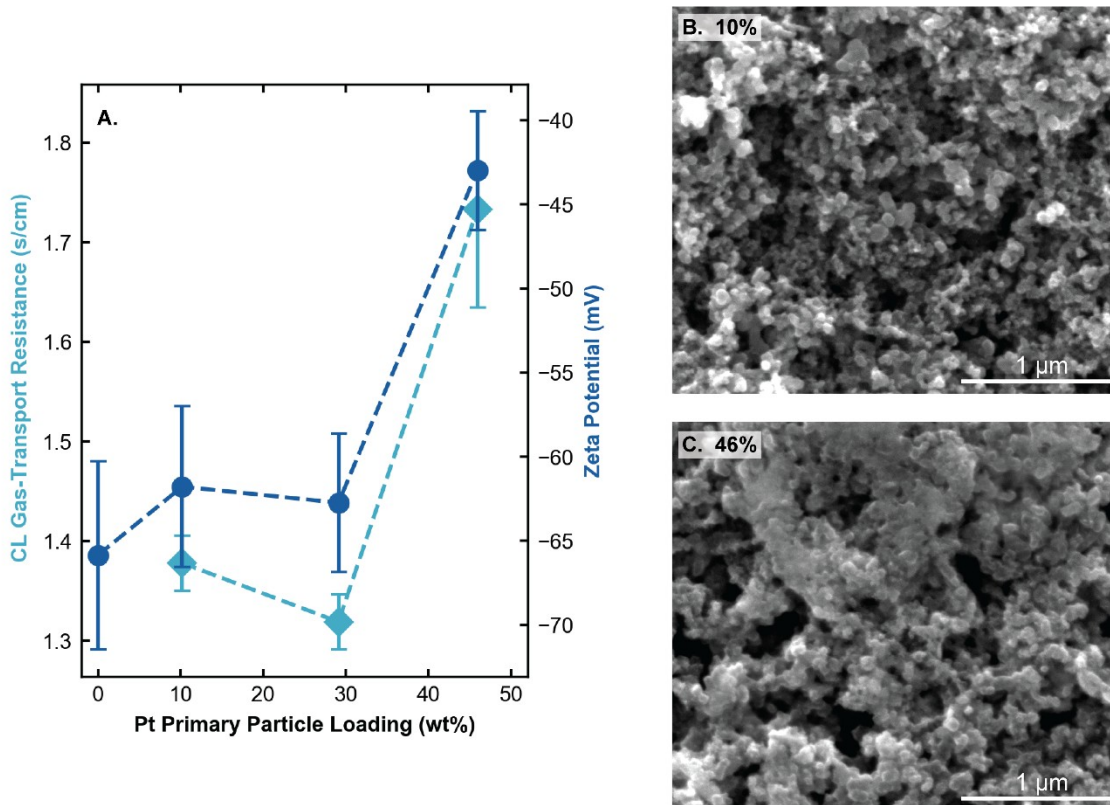


Figure 3. (A.) Gas-transport resistance of catalyst layers (CLs) containing the same total platinum loading (0.05 mg/cm^2), but varying primary particle platinum loading. The zeta potentials of the inks used to cast these CLs are also shown. Scanning electron microscopy images of CLs manufactured with (B.) 10 wt% Pt/C and (C.) 46 wt% Pt/C (the same samples measured as in (A.)). Error bars display the standard deviation of multiple replicate samples.

From the ζ -potential measurements at low PPL, we expect the majority of ionomer to adsorb to the carbon support particles because the surface is not adsorption saturated (*i.e.*, an I:C of 0.7 is on the left side of the U-shaped ζ -potential curve). At high PPL, we conversely expect some free ionomer in solution, because the I:C ratio is past the ζ -potential transition value. Non-uniform ionomer distribution over the catalyst-particle surface due to reduced carbon SA at high PPL correlates with the increased local transport resistances observed in Figure 3A.

Both low-magnitude ζ -potential and high gas-transport resistances indicate microstructural changes of the CL, likely larger agglomerates. A lower magnitude ζ -potential demands less repulsion between the catalyst particles in the ink. This likely results in larger agglomerates, and in turn, increases the local transport resistance due to the more tortuous pathways the gas must take to reach buried platinum within the aggregates. To verify this hypothesis and study the structure, SEM was used to image the CLs as shown in Figure 3B-C for CLs fabricated with PPL of 10 and 46 Pt wt.%, respectively. The 10 wt.% sample exhibits a highly dispersed porous structure with well-distributed pores, whereas the 46 Pt wt.% sample displays a more aggregated structure, in agreement with the gas-transport resistance and ζ -potential data. While these representative images do not reveal the ionomer distribution within the CL, they do indicate structural changes across the different PPLs, likely caused by changes in ionomer distributions. Indeed at this time, no technique is able to resolve 3-dimensional ionomer structure in CLs with sufficient chemical and spatial resolution, though reconstructions have been accomplished in the absence of platinum⁸. Such technique development is beyond the scope of this work, and we instead use the electrochemical measurements below to corroborate the hypothesis of PPL impacting ionomer distribution in the CL.

Double-layer capacitance (C_{dl}) can also ascertain ionomer distribution within the CL, as previously described.²⁴ Briefly, under partially dry conditions only the agglomerate surface covered by ionomer contributes to C_{dl} . Under more wet conditions, the entire surface of the

agglomerate likely contributes to C_{dl} due to the presence of both water and ionomer pathways. Capacitive measurements are related to ionomer coverage; the dry-to-wet ratio of C_{dl} is indicative of the fraction of catalyst-particle surface area covered by ionomer (though there may not be a strictly linear relationship due to differences in the dielectric permittivity of hydrated versus dry Nafion). When this measurement is repeated with CO (adsorbed on Pt), the capacitance is attributed primarily to carbon, assuming that adsorbed CO generally insulates the platinum SA.²⁴ The Pt-capacitance contribution under dry and wet conditions is isolated by subtracting the C_{dl} with CO adsorbed from the total C_{dl} . The results are presented in Figure 4. Note that these data are related to the percentage surface of carbon and platinum, respectively, covered by ionomer, and that the two values should not necessarily sum to one (*i.e.*, both could be unity).

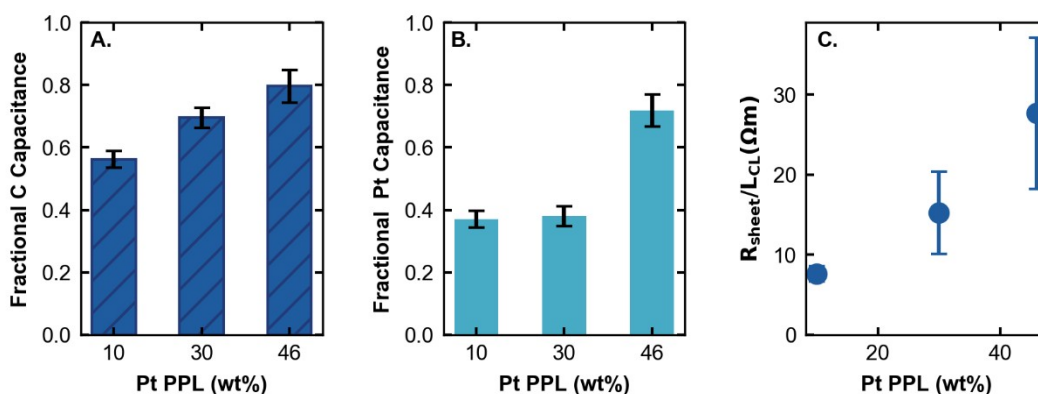


Figure 4. Fractional (A.) carbon and (B.) platinum double-layer capacitance due to ionomer coverage on those respective surfaces. (C.) Bulk catalyst layer (CL) sheet resistance (R_{CL}) at 100% RH, normalized by thickness of the CL (L_{CL}). All data are for electrodes containing 0.1 mg/cm² platinum loading, achieved while varying the Pt PPL. Error bars display the standard deviation of multiple replicate samples.

The ionomer coverage on carbon is within a small range across all samples, suggesting similar ionomer/carbon interactions across all samples. Nevertheless, there is a clear monotonic increase

in fractional carbon capacitance as PPL increases (Figure 4A). Concurrently, the total carbon surface area available for ionomer to interact with steadily decreases as PPL increases. Because the available carbon surface area decrease from the surface area calculation in the SI is larger than the capacitance increase measured in Figure 4, the overall amount of ionomer adsorbed to C falls with increased PPL, consistent with ζ -potential predictions. This trend is also consistent with the hypothesis that the overall carbon-support-particle surface is more adsorption saturated at larger PPL (due to lower total available carbon surface area at a fixed I:C).

The Pt fractional capacitance exhibits a sharp change in magnitude between 30 and 46% Pt PPL, which is coincident with the ζ -potential measurements (because the 46% is to the right of the U-bend in Figure 1). A higher coverage on Pt at higher PPL is not evident from ink ζ -potential or prior adsorption studies.³² This trend could be due to spillover from adsorption onto carbon. Alternatively, higher ionomer coverage on Pt at high PPL could potentially result from the drying step in CL fabrication. As the solvent evaporates, free solution ionomer (for high PPL samples that are on the right side of the U-shaped ζ -potential curve) deposits on available free surface area (including Pt surface area). Such induced deposition in a relatively fast drying step that occurs during spray deposition can result in non-uniform ionomer distribution or isolated ionomer aggregates, in agreement with the SEM images (**Figure 3B-C**). A similar result would not be expected in a slow-drying deposition method, such as blade coating. The ionomer drying-deposition mechanism may yield poor ionic conductivity, especially when combined with the heterogeneous ionomer distribution on the catalyst-particle agglomerate surface from adsorbed ionomer. However, in some cases a heterogeneous structure may be desirable, and more detailed studies on how deposition conditions affect CL structure are required.

Poor conductivity is consistent with observed high CL sheet resistance (R_{sheet}) at high PPL in **Figure 4C** measured at 100% RH. CL R_{sheet} measures through-plane H^+ transport resistance. Since high PPL CLs are thinner at fixed nominal Pt loadings (0.1 mg/cm^2), CL R_{sheet} values are normalized in **Figure 4C** by the thickness of CL (L_{CL}) cross sections measured by SEM (summarized in Table S5). When normalized by the CL thickness, differences in R_{sheet} are a direct result of changes in ionomer distribution (because the ionomer should have the same intrinsic conductivity in all electrodes and at the same amount assuming similar ionomer thin-film

thicknesses, discussed further in the SI). A high R_{sheet}/L_{CL} suggests a heterogeneous ionomer distribution with poor ionomer connectivity, such as ionomer aggregates connected by thin ionomer strands and/or a highly tortuous ionomer network.

It is important to note, however, that despite the larger normalized resistances (Figure 3A and Figure 4C), higher PPLs allow for thinner electrodes that reduce the total through-plane gas and H^{+i} -transport resistance and allow for higher Pt utilization throughout the CL thickness. These nominal resistance values may be more important than normalized values for dictating performance under certain PEFC operating conditions with high water production. Polarization-curve plots (corrected by multiplying with the sample r_f and dividing by average r_f , both measured at operating RH) in Figure 5 demonstrate superior performance of CLs with higher PPL compared to 10 wt.% PPL, likely due to the thickness differences (Table S5). This is consistent with pore-scale modeling results.⁴⁵ CLs with 30 wt.% PPL seem to provide the optimal CL structure, balancing the local and through-plane transport resistances, and thus providing the best performance. Trade-offs between local interactions and macroscopic processes must both be considered.

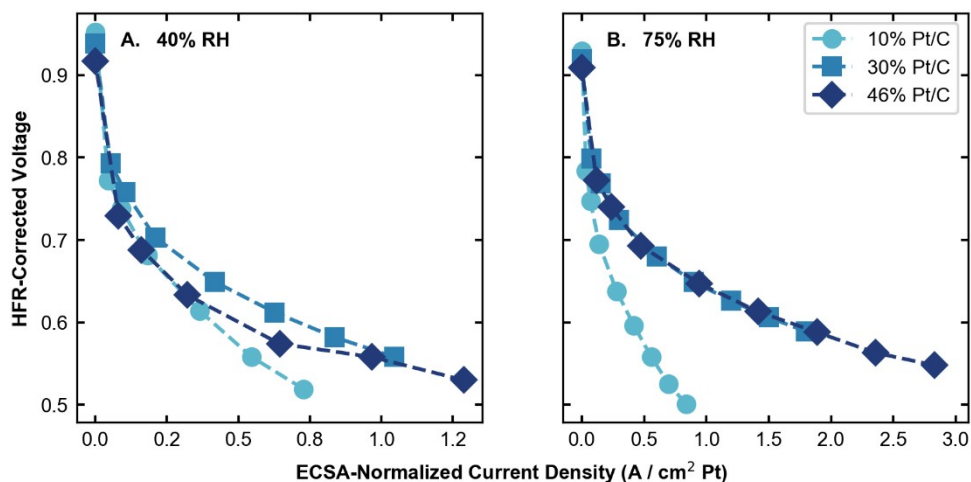


Figure 5. H_2 -Air polarization curves obtained from CLs using different PPL on the WE, with a total Pt loading of 0.1 mg/cm². Operating conditions were 80°C, 150 kPa backpressure, and

either (A.) 40% relative humidity (RH) or (B.) 75% RH. The voltage is corrected for high-frequency ohmic resistance (HFR), and the current density is normalized to Pt specific surface area.

Our results agree with prior studies in which low PPL catalysts demonstrated superior current-voltage behavior when CL thickness was held constant across all samples by carbon dilution, likely due to improved local transport.⁴⁴ Even when polarization curves are corrected for ohmic resistance and hydrogen crossover, low PPLs still demonstrate better performance, confirming that the polarization-curve differences arise because of changing local transport resistances. However, Schuler *et al.* did not observe much impact of PPL on local resistance likely because they used a high-surface-area carbon support wherein a significant fraction of Pt nanoparticles are located in interior micropores.² Thus, the carbon-versus-platinum exterior surface area is not significantly impacted by PPL for these types of catalyst particles. This observation again highlights the interplay between various CL parameters such as PPL and carbon support type and the need to account for all CL parameters to achieve optimal CL design/structure. We also note that our CLs were fabricated with a fixed I:C ratio that highlights the influence of ionomer/particle interactions across the PPL range studied; if this same PPL range was fabricated with all very low or very high I:C ratios such that all inks were on one side of the U-shaped curve, we expect the trends to be dominated by intrinsic ionomer properties at these I:C ratio extremes, rather than by ionomer/particle interactions.

Finally, we emphasize that our paper reveals how changing PPL impacts CL gas-transport performance. SEM imaging suggests changes in microstructure. Through zeta potential, pH, and capacitance measurements, the likely conclusion is that the differences between the different PPL CLs are caused by changes in ionomer distributions. However, to confirm this hypothesis, advancements in microscopy and spectroscopy techniques must be made to image ionomer distributions with actual CLs.

CONCLUSIONS

Inks for PEFC catalyst layers (CLs) consist of solvent, ionomer, and catalyst particles, and colloidal interactions among these components can critically influence CL microstructure and therefore, polarization performance. In this study, the impact of platinum primary particle loading (PPL) on catalyst-particle/ionomer ink interactions and subsequent effects on CL microstructure and thus gas- and H^{+} -transport resistance was explored. Previous work demonstrated that Nafion ionomer preferentially adsorbs to carbon surfaces in inks, rather than to platinum. Here, we find that as PPL is increased and the available carbon surface area decreases, the carbon surface saturates at a lower ionomer content and additional non-adsorbed ionomer remains dispersed in the solvent. More free ionomer in the solution results in higher ionic strength, lower magnitude ink ζ -potentials and, thus, a more agglomerated CL microstructure. These trends agree with results from ink ζ -potential and pH measurements, SEM imaging, and CL capacitance measurements. Non-adsorbed ionomer can deposit non-uniformly during the CL fabrication process, resulting in observed poor H^{+} conductivity. Hence, low PPL catalysts are preferred to improve local transport processes. However, higher PPL catalysts with low CL thickness are advantageous with respect to reducing through-plane reactant gas- and H^{+} -transport resistances, thereby providing better Pt utilization. These two different transport resistances (local and bulk) need to be optimized, and this optimum point undoubtedly varies depending on target operating conditions. Additionally, I:C ratio is a critical parameter that is dependent on PPL. There is no one optimal I:C ratio, it instead depends on the specific ink conditions and how the ionomer interacts with the catalyst particles. Based on our results, moderate PPLs with I:C ratios where the ζ -potential magnitude is maximized, may provide an optimal balance between all of the effects studied here. Of note, the ionomer/catalyst-particle interactions probed here are known to depend on solvent composition, highlighting the large ink variable space that can be manipulated to alter CL structure. Further studies are required to understand this parameter space and its impact on final CL performance, including the delineation between local and macroscopic properties. Importantly, this study demonstrates a direct link between ink interactions and CL performance metrics, revealing critical insights into how ionomer coverage and transport processes are affected by carbon and platinum surface

areas. Such information is imperative to optimize inks for enhanced CL transport and improved platinum utilization in PEFC applications.

ASSOCIATED CONTENT

Supporting Information. Additional details of the experimental methods, additional pH and zeta potential data, SEM cross sections of the different catalyst layers, surface area calculations.

ACKNOWLEDGEMENTS

The authors would like to thank Dr. David Cullen and Dr. Elliot Padgett for helpful discussions about Pt/C surface areas. This material is primarily based on work performed by the Million Mile Fuel Cell Truck (M2FCT) Consortium (<https://millionmilefuelcelltruck.org>), technology manager Greg Kleen, which is supported by the U.S. Department of Energy, Office of Energy Efficiency and Renewable Energy, Hydrogen and Fuel Cell Technologies Office, under contract number DE-AC02-05CH1123, with initial funding from the Fuel Cell Performance and Durability Consortium (FC-PAD) under the same contract. S.A.B acknowledges support from the Graduate Research Fellowship Program by the National Science Foundation under Grant No. DGE 1752814.

REFERENCES

1. Weber, A. Z.; Kusoglu, A., Unexplained Transport Resistances for Low-Loaded Fuel-Cell Catalyst Layers. *J. Mater. Chem. A* **2014**, *2* (41), 17207-17211.
2. Schuler, T.; Chowdhury, A.; Freiberg, A. T.; Sneed, B.; Spingler, F. B.; Tucker, M. C.; More, K. L.; Radke, C. J.; Weber, A. Z., Fuel-Cell Catalyst-Layer Resistance via Hydrogen Limiting-Current Measurements. *J. Electrochem. Soc.* **2019**, *166* (7), F3020-F3031.
3. Karan, K., PEFC Catalyst Layer: Recent Advances in Materials, Microstructural Characterization, and Modeling. *Current Opinion in Electrochemistry* **2017**, *5* (1), 27-35.
4. Holdcroft, S., Fuel Cell Catalyst Layers: A Polymer Science Perspective. *Chem. Mater.* **2014**, *26* (1), 381-393.
5. Xie, J.; Wood, D. L.; More, K. L.; Atanassov, P.; Borup, R. L., Microstructural Changes of Membrane Electrode Assemblies during PEFC Durability Testing at High Humidity Conditions. *J. Electrochem. Soc.* **2005**, *152* (5), A1011.
6. More, K.; Borup, R.; Reeves, K., Identifying Contributing Degradation Phenomena in PEM Fuel Cell Membrane Electrode Assemblies Via Electron Microscopy. *ECS Trans.* **2019**, *3* (1), 717-733.
7. Lei, C.; Yang, F.; Macauley, N.; Spinetta, M.; Purdy, G.; Jankovic, J.; Cullen, D. A.; More, K. L.; Kim, Y. S.; Xu, H., Impact of Catalyst Ink Dispersing Solvent on PEM Fuel Cell Performance and Durability. *J. Electrochem. Soc.* **2021**, *168* (4), 044517.
8. Lopez-Haro, M.; Guétaz, L.; Printemps, T.; Morin, A.; Escribano, S.; Jouneau, P. H.; Bayle-Guillemaud, P.; Chandezon, F.; Gebel, G., Three-dimensional Analysis of Nafion Layers in Fuel Cell Electrodes. *Nature Communications* **2014**, *5*, 5229.
9. Morawietz, T.; Handl, M.; Oldani, C.; Friedrich, K. A.; Hiesgen, R., Quantitative in Situ Analysis of Ionomer Structure in Fuel Cell Catalytic Layers. *ACS Applied Materials & Interfaces* **2016**, *8* (40), 27044-27054.
10. Wu, J.; Melo, L. G. A.; Zhu, X.; West, M. M.; Berejnov, V.; Susac, D.; Stumper, J.; Hitchcock, A. P., 4D Imaging of Polymer Electrolyte Membrane Fuel Cell Catalyst Layers by Soft X-ray Spectro-Tomography. *J. Power Sources* **2018**, *381*, 72-83.
11. Wu, J.; Zhu, X.; West, M. M.; Tyliszczak, T.; Shiu, H.-W.; Shapiro, D.; Berejnov, V.; Susac, D.; Stumper, J.; Hitchcock, A. P., High-Resolution Imaging of Polymer Electrolyte Membrane Fuel Cell Cathode Layers by Soft X-ray Spectro-Ptychography. *J. Phys. Chem. C* **2018**, *122* (22), 11709-11719.
12. Cetinbas, F. C.; Ahluwalia, R. K.; Kariuki, N. N.; Myers, D. J., Agglomerates in Polymer Electrolyte Fuel Cell Electrodes: Part I. Structural Characterization. *J. Electrochem. Soc.* **2018**, *165* (13), F1051-F1058.
13. Litster, S.; Epting, W. K.; Wargo, E. A.; Kalidindi, S. R.; Kumbur, E. C., Morphological Analyses of Polymer Electrolyte Fuel Cell Electrodes with Nano-Scale Computed Tomography Imaging. *Fuel Cells* **2013**, *13* (5), 935-945.
14. Cetinbas, F. C.; Ahluwalia, R. K.; Kariuki, N.; De Andrade, V.; Fongalland, D.; Smith, L.; Sharman, J.; Ferreira, P.; Rasouli, S.; Myers, D. J., Hybrid Approach

Combining Multiple Characterization Techniques and Simulations for Microstructural Analysis of Proton Exchange Membrane Fuel Cell Electrodes. *J. Power Sources* **2017**, 344, 62-73.

15. Greszler, T. A.; Caulk, D.; Sinha, P., The Impact of Platinum Loading on Oxygen Transport Resistance. *J. Electrochem. Soc.* **2012**, 159 (12), F831-F840.

16. Sasikumar, G.; Ihm, J. W.; Ryu, H., Optimum Nafion Content in PEM Fuel Cell Electrodes. *Electrochim. Acta* **2004**, 50 (2-3), 601-605.

17. Orfanidi, A.; Madkikar, P.; El-Sayed, H. A.; Harzer, G. S.; Kratky, T.; Gasteiger, H. A., The Key to High Performance Low Pt Loaded Electrodes. *J. Electrochem. Soc.* **2017**, 164 (4), F418-F426.

18. Ishikawa, H.; Sugawara, Y.; Inoue, G.; Kawase, M., Effects of Pt and Ionomer Ratios on the Structure of Catalyst Layer: A Theoretical Model for Polymer Electrolyte Fuel Cells. *J. Power Sources* **2018**, 374, 196-204.

19. Padgett, E.; Andrejevic, N.; Liu, Z.; Kongkanand, A.; Gu, W.; Moriyama, K.; Jiang, Y.; Kumaraguru, S.; Moylan, T.; Kukreja, R.; Muller, D., Connecting Fuel Cell Catalyst Nanostructure and Accessibility Using Quantitative Cryo-STEM Tomography. *J Electrochem Soc* **2018**, 165 (3), F173-F180.

20. Sneed, B. T.; Cullen, D. A.; Reeves, K. S.; Dyck, O. E.; Langlois, D. A.; Mukundan, R.; Borup, R. L.; More, K. L., 3D Analysis of Fuel Cell Electrocatalyst Degradation on Alternate Carbon Supports. *Acs Appl Mater Inter* **2017**, 9 (35), 29839-29848.

21. Berlinger, S. A.; Garg, S.; Weber, A. Z., Multicomponent, Multiphase Interactions in Fuel-Cell Inks. *Current Opinion in Electrochemistry* **2021**, 29, 100744.

22. Hatzell, K. B.; Dixit, M. B.; Berlinger, S. A.; Weber, A. Z., Understanding Inks for Porous-Electrode Formation. *J. Mater. Chem. A* **2017**, 5 (39), 20527-20533.

23. Dixit, M. B.; Harkey, B. A.; Shen, F.; Hatzell, K. B., Catalyst Layer Ink Interactions That Affect Coatability. *J. Electrochem. Soc.* **2018**, 165 (5), F264-F271.

24. Van Cleve, T.; Khandavalli, S.; Chowdhury, A.; Medina, S.; Pylypenko, S.; Wang, M.; More, K. L.; Kariuki, N. N.; Myers, D. J.; Weber, A. Z.; Mauger, S.; Ulsh, M.; Neyerlin, K. C., Dictating Pt-based Electrocatalyst Performance in Polymer Electrolyte Fuel Cells; from Formulation to Application. *ACS Appl. Mater. Interfaces* **2019**.

25. Kim, T.-H.; Yi, J.-Y.; Jung, C.-Y.; Jeong, E.; Yi, S.-C., Solvent Effect on the Nafion Agglomerate Morphology in the Catalyst Layer of the Proton Exchange Membrane Fuel Cells. *Int. J. Hydrogen Energy* **2017**, 42 (1), 478-485.

26. Orfanidi, A.; Rheinländer, P. J.; Schulte, N.; Gasteiger, H. A., Ink Solvent Dependence of the Ionomer Distribution in the Catalyst Layer of a PEMFC. *J. Electrochem. Soc.* **2018**, 165 (14), F1254-F1263.

27. Sharma, R.; Grahl-Madsen, L.; Andersen, S. M., Influence of Dispersion Media on Nafion® Ionomer Distribution in Proton Exchange Membrane Fuel Cell Catalyst Carbon Support. *Materials Chemistry and Physics* **2019**, 226, 66-72.

28. Balu, R.; Choudhury, N. R.; Mata, J. P.; de Campo, L.; Rehm, C.; Hill, A. J.; Dutta, N. K., Evolution of the Interfacial Structure of a Catalyst Ink with the Quality of the Dispersing Solvent: A Contrast Variation Small-Angle and Ultrasmall-Angle Neutron Scattering Investigation. *ACS Appl. Mater. Interfaces* **2019**, *11* (10), 9934-9946.
29. Woo, S.; Lee, S.; Taning, A. Z.; Yang, T.-H.; Park, S.-H.; Yim, S.-D., Current Understanding of Catalyst/Ionomer Interfacial Structure and Phenomena Affecting the Oxygen Reduction Reaction in Cathode Catalyst Layers of Proton Exchange Membrane Fuel Cells. *Current Opinion in Electrochemistry* **2020**, *21*, 289-296.
30. Chowdhury, A.; Bird, A.; Liu, J.; Zenyuk, I. V.; Kusoglu, A.; Radke, C. J.; Weber, A. Z., Linking Perfluorosulfonic Acid Ionomer Chemistry and High-Current Density Performance in Fuel-Cell Electrodes. *ACS Appl. Mater. Interfaces* **2021**, *13* (36), 42579-42589.
31. Khandavalli, S.; Park, J. H.; Kariuki, N. N.; Myers, D. J.; Stickel, J. J.; Hurst, K.; Neyerlin, K. C.; Ulsh, M.; Mauger, S. A., Rheological Investigation on the Microstructure of Fuel Cell Catalyst Inks. *ACS Appl. Mater. Interfaces* **2018**, *10* (50), 43610-43622.
32. Berlinger, S. A.; McCloskey, B. D.; Weber, A. Z., Probing Ionomer Interactions with Electrocatalyst Particles in Solution. *ACS Energy Letters* **2021**, 2275-2282.
33. Xie, B.; Zhang, G.; Xuan, J.; Jiao, K., Three-dimensional Multi-Phase Model of PEM Fuel Cell Coupled with Improved Agglomerate Sub-model of Catalyst Layer. *Energy Conversion and Management* **2019**, *199*, 112051.
34. Berlinger, S. A.; McCloskey, B. D.; Weber, A. Z., Inherent Acidity of Perfluorosulfonic Acid Ionomer Dispersions and Implications for Ink Aggregation. *J. Phys. Chem. B* **2018**, *122* (31), 7790-7796.
35. Ono, Y.; Ohma, A.; Shinohara, K.; Fushinobu, K., Influence of Equivalent Weight of Ionomer on Local Oxygen Transport Resistance in Cathode Catalyst Layers. *J Electrochem Soc* **2013**, *160* (8), F779-F787.
36. Schuler, T.; Chowdhury, A.; Freiberg, A. T. S.; Sneed, B. T.; Spingler, F. B.; Tucker, M. C.; More, K.; Radke, C. J.; Weber, A. Z., Fuel-Cell Catalyst-Layer Resistance via Hydrogen Limiting-Current Measurements. *J Electrochem Soc* **2019**, *166* (7), F3020-F3031.
37. Iden, H.; Ohma, A., An in situ Technique for Analyzing Ionomer Coverage in Catalyst Layers. *J. Electroanal. Chem.* **2013**, *693*, 34-41.
38. Spingler, F. B.; Phillips, A.; Schuler, T.; Tucker, M. C.; Weber, A. Z., Investigating Fuel-Cell Transport Limitations using Hydrogen Limiting Current. *Int J Hydrogen Energ* **2017**, *42* (19), 13960-13969.
39. Diard, J.-P.; Le Gorrec, B.; Montella, C., *Handbook of Electrochemical Impedance Spectroscopy. DIFFUSION IMPEDANCES*. 2020.
40. Open Source Impedance Fitter. <https://github.com/NREL/OSIF>. Accessed on June 1, 2022
41. Israelachvili, J. N., *Intermolecular and Surface Forces*. Academic Press: 2011; Vol. 3.

42. Sondheimer, S. J.; Bunce, N. J.; Lemke, M. E.; Fyfe, C. A., Acidity and Catalytic Activity of Nafion-H. *Macromolecules* **1986**, *19* (2), 339-343.
43. Thoma, M.; Lin, W.; Hoffmann, E.; Sattes, M.; Segets, D.; Damm, C.; Peukert, W., A Simple and Reliable Method for Studying the Adsorption Behavior of Aquivion® Ionomers on Carbon Black Surfaces. *Langmuir* **2018**, *34* (41), 12324-12334.
44. Owejan, J. P.; Owejan, J. E.; Gu, W., Impact of Platinum Loading and Catalyst Layer Structure on PEMFC Performance. *J Electrochem Soc* **2013**, *160* (8), F824-F833.
45. Hou, Y.; Deng, H.; Pan, F.; Chen, W.; Du, Q.; Jiao, K., Pore-scale Investigation of Catalyst Layer Ingredient and Structure Effect in Proton Exchange Membrane Fuel Cell. *Applied Energy* **2019**, *253*, 113561.

TOC GRAPHIC

Ink interactions impact the fuel-cell Catalyst Layer

